ESTIMATES OF SMALL–SCALE HORIZONTAL DIVERGENCE AND RELATIVE VORTICITY IN THE OCEAN

Ren–Chieh Lien and Peter Müller

Department of Oceanography
School of Ocean and Earth Science and Technology
University of Hawaii at Manoa
Honolulu, Hawaii 96822

ABSTRACT

An attempt to estimate horizontal divergence and the vertical component of relative vorticity at small scales is made using measurements from Internal Wave Experiment. These two quantities are very useful to decompose the small–scale motion into the vortical and gravity modes. Fluctuations of horizontal divergence and relative vorticity estimated using a three–point array are found to be attenuated and mutually contaminated at small horizontal scales. Assuming a horizontal isotropy condition, these sampling errors can be represented as two array response functions which act as horizontal wavenumber spectral windows imposing on wavenumber–frequency spectra of horizontal divergence and relative vorticity. Examining effects of array response functions for the GM–76 spectrum suggests that both the attenuation and contamination effects must be considered in obtaining the relative vorticity spectrum, whereas only the attenuation effect is important for the horizontal divergence spectrum since the contamination from relative vorticity is negligible.

INTRODUCTION

Small-scale motions in the ocean consist of both gravity waves and vortical motion. The vortical motion is distinguished from gravity waves by carrying the perturbation potential vorticity in the system. Therefore, it is likely that small-scale vortical motion plays an important role in the enstrophy (variance of potential vorticity) cascade in the ocean.

A normal mode decomposition scheme was proposed by Müller (1984) to project small-scale oceanic motion into the gravity and vortical modes. It can be achieved most conveniently using fields of horizontal divergence, the vertical component of relative vorticity, and vortex stretching (Lien, 1990). Attempts to estimate these three fields at small scales in the ocean have been made using measurements from Internal Wave Experiment (IWEX; Briscoe, 1975) by Müller et al. (1988) and by Lien (1990). Estimates

of "area–averaged" horizontal divergence and relative vorticity were obtained using spatially discrete velocity measurements.

It was pointed out by Prater (1989) and Kunze et al. (1990) that the three–point array of IWEX will detect "relative vorticity" even in a pure horizontal divergence flow field (free of relative vorticity). This paper examines potential errors of estimates of horizontal divergence and relative vorticity. The estimation of horizontal divergence and relative vorticity at small scales using IWEX measurements is described in the following section. Next, their spectral analysis, associated array response functions, and their effects for the GM–76 spectrum model are discussed. Conclusions are summarized in the last section.

ESTIMATES OF HORIZONTAL DIVERGENCE (HD) AND RELATIVE VORTICITY (RV)

An attempt to separate small–scale oceanic fluctuations into the gravity and vortical modes can be achieved conveniently using fields of HD, RV, and VS at small scales. To estimate these fields requires oceanic measurements of horizontal velocity and temperature with a sufficient spatial resolution. Oceanic measurements from IWEX seem to be suitable for such calculations.

The IWEX was conducted in late 1973 over a 42-day period. A trimooring array was designed on which 20 current meters (17 VACM and 3 EG&G 850) and temperature sensors were deployed in the main thermocline of the Sargasso Sea (27°44′ N, 69°51′ W). Horizontal velocity components, temperature, and temperature difference over a vertical distance of 1.74 m were measured. Horizontal spacing between sensors ranged from 1.4 m to 1600 m and vertical spacing from 2.1 m to 1447 m. Sampling interval was 225 s, except at the lowest level (2050 m depth) which was sampled every 900 s. The trimooring array was a nearly perfect tetrahedron (roughly 6 km on a side) with the apex at the top of the main thermocline at 604 m depth and the deepest current meter and temperature sensor at a depth of 2050 m. A schematic diagram of IWEX is shown in Figure 1. The mooring was very stable during the entire experiment. Pressure records showed ±0.2 m displacement at the apex and about ±6 m at 3000 m. A detailed description of IWEX was given by Tarbell et al. (1976). The IWEX measurements provide an opportunity to estimate spatial gradients in the time and space scales of small–scale motions. Measurements from 15 current meters and temperature sensors are used at five horizontal planes where measurements are available at all three legs. Characteristics of the five IWEX levels are described in Table 1.

Area–averaged horizontal divergence $\overline{HD}$ and relative vorticity $\overline{RV}$ can be obtained from velocity measurements on a horizontal plane using Stokes' and Gauss' theorems as

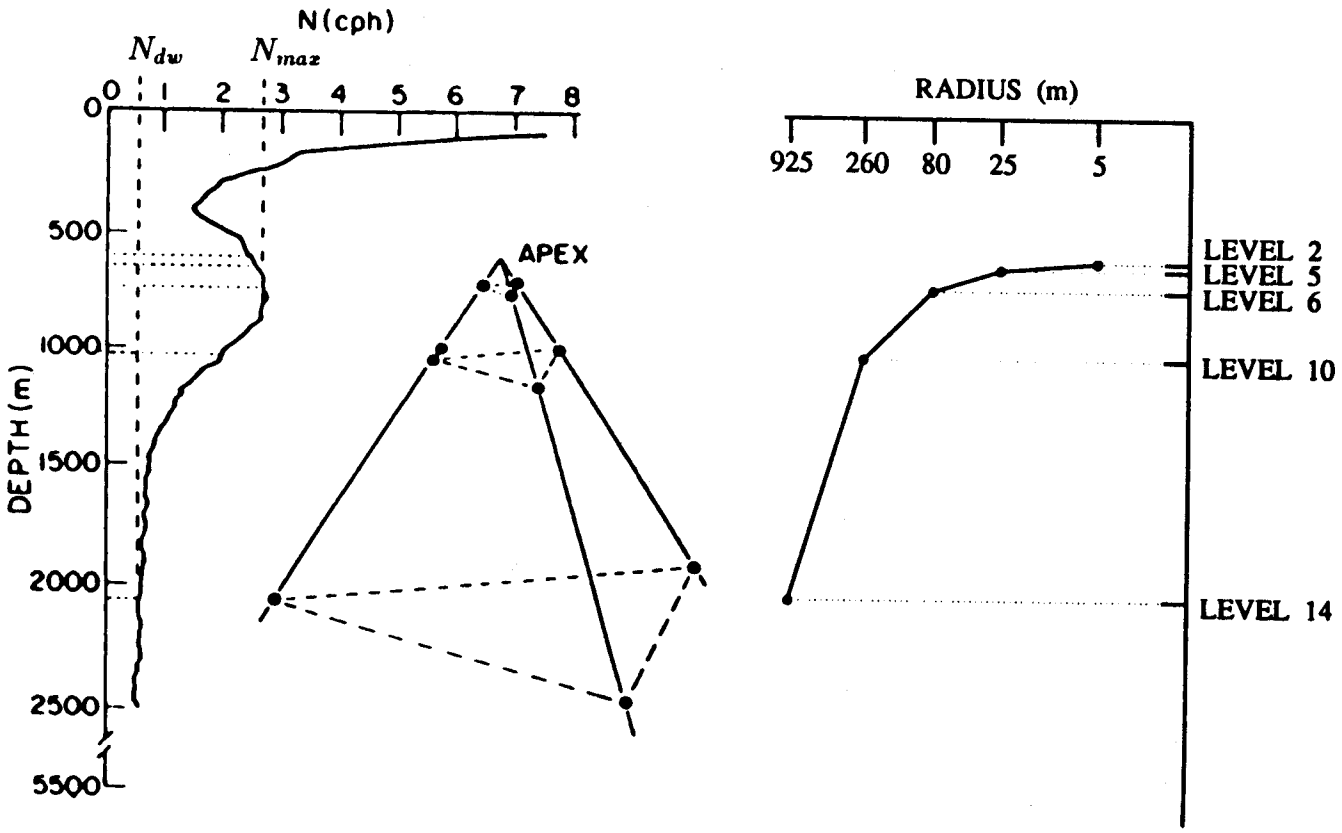

Figure 1. Schematic view of the geometry of the IWEX array and profiles of the Brunt-Väisälä frequency $N(z)$ and horizontal radius $R(z)$. Points indicate current meter positions. There are ten more current meters near the apex which are not shown. The levels that contain three current meters are indicated. The maximum Brunt-Väisälä frequency in the main thermocline is $N_{max} = 2.76$ cph. In the deep water column below 2050 m, N is almost constant, $N_{dw} = 0.36$ cph.

$$\overline{HD} = \frac{1}{A} \oint \underline{u} \cdot d\underline{n}, \tag{1}$$

$$\overline{RV} = \frac{1}{A} \oint \underline{u} \cdot d\underline{t}. \tag{2}$$

Here $\underline{t}$ and $\underline{n}$ are the tangential and the normal unit vectors along the circumference of an area A, and $\underline{u}$ is the horizontal velocity vector.

Assuming N velocity sensors ($N = 3$ for IWEX trimooring array) evenly located on a circle on a horizontal plane (Figure 2), $\overline{HD}$ and $\overline{RV}$ are estimated by approximating the circle integration by a discrete sum of the radial and normal velocity components along the circle, i.e.,

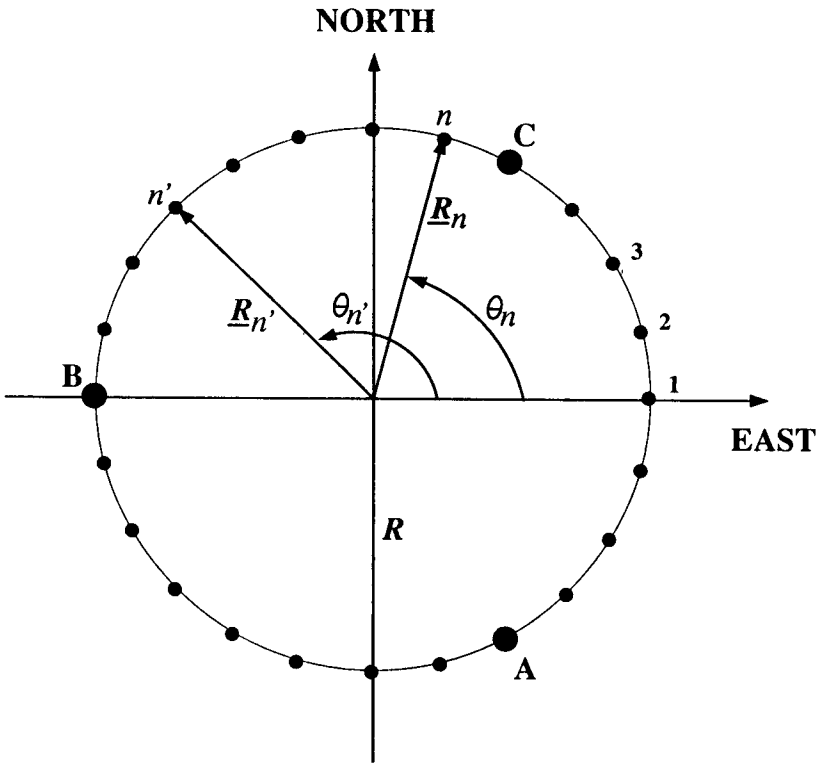

Figure 2. Configuration of N current sensors evenly located on a circle at a horizontal plane. Three larger dots, indexed by A, B, and C, denote positions of current sensors on the IWEX trimooring array. The radius of the circle is R, θ is the orientation of the current sensor counterclockwise from the east, and $\underline{R}$ is the corresponding position vector.

Table 1. Characteristics of five IWEX levels with three current meters

Level	Depth (m)	Radius (m)	N (cph)	Number of sampling
2	606	4.9	2.54	1800
5	640	25.4	2.60	12000
6	731	80.3	2.76	12000
10	1023	260.0	2.05	4800
14	2050	925.0	0.66	3900

$$\overline{HD} = \frac{1}{\pi R^2} \sum_{n=1}^{N} u_r^{(n)} \frac{2\pi R}{N}, \tag{3}$$

$$\overline{RV} = \frac{1}{\pi R^2} \sum_{n=1}^{N} u_t^{(n)} \frac{2\pi R}{N}, \tag{4}$$

where R is the radius of the circle, and $u_r^{(n)}$ and $u_t^{(n)}$ are the radial and normal velocity components of the n^{th} sensor defined as

$$u_r^{(n)} = u_r(R, \theta_n) = u(R, \theta_n) cos(\theta_n) + v(R, \theta_n) sin(\theta_n), \tag{5}$$

$$u_t^{(n)} = u_t(R, \theta_n) = -u(R, \theta_n) sin(\theta_n) + v(R, \theta_n) cos(\theta_n). \tag{6}$$

Here, θ_n is the angle counterclockwise from the east of the n^{th} current sensor. For the IWEX trimooring array, area-averaged horizontal divergence $\overline{HD}$ and relative vorticity $\overline{RV}$ are estimated as

$$\overline{HD} = \frac{2}{3R} \left(\frac{u_A + u_C}{2} - u_B \right) + \frac{1}{\sqrt{3}R} (v_C - v_A), \tag{7}$$

$$\overline{RV} = \frac{2}{3R} \left(\frac{v_A + v_C}{2} - v_B \right) - \frac{1}{\sqrt{3}R} (u_C - u_A). \tag{8}$$

Alternatively, $\overline{HD}$ and $\overline{RV}$ can be obtained using velocity gradients estimated from the least squares fitting of horizontal velocity measurements. These two approaches are found to be equivalent. Time series of $\overline{HD}$ and $\overline{RV}$ at five different depths of IWEX are obtained. Applying the run test and the goodness test, the time series of $\overline{HD}$ and $\overline{RV}$ are found to be stationary and Gaussian distributed (Lien, 1990).

SPECTRAL ANALYSIS OF $\overline{HD}$ and $\overline{RV}$

Time series of $\overline{HD}$ and $\overline{RV}$ are first divided into segments with a length of 1024 (2^{10}) data points. Successive segments are 50% overlapped. Each segment is subjected to a Hanning window and is fast Fourier transformed. The one-sided spectrum, averaged over all segments, is further averaged over adjacent frequency components resulting in 40 frequency points spaced about equally on a logarithmic scale.

Measurement errors on estimates of $\overline{HD}$ and $\overline{RV}$ have been discussed by Müller et al. (1988). Variance due to the instrumental noise can be estimated by separating velocity measurements at level 2 (R = 4.9 m) into coherent signal and incoherent noise components. At level 2, observed frequency spectra of $\overline{HD}$ and $\overline{RV}$ are dominated by the incoherent noise component and will be excluded from our analysis. At other levels, variance due to incoherent noise is removed from the frequency spectral estimates of $\overline{HD}$ and $\overline{RV}$.

Frequency spectra of $\overline{HD}$ and $\overline{RV}$ at levels 5, 6, 10, and 14 are displayed in Figures 3 and 4. Frequency spectra $S_{\overline{HD}}(\omega)$ and $S_{\overline{RV}}(\omega)$ are of the same order at each level and decrease systematically with increasing radius or depth.

Array Response Function

If $\overline{HD}$ and $\overline{RV}$ are obtained from N velocity measurements located on a circle with a radius R, their frequency spectral estimates $S_{\overline{HD}}(\omega; R, N)$ and $S_{\overline{RV}}(\omega; R, N)$ do not represent exactly area–averaged frequency spectra of horizontal divergence and relative vorticity.

Area–averaged horizontal divergence $\overline{HD}$ can be expressed in terms of Fourier transforms as

$$\overline{HD} = \frac{2}{NR}\sum_{n=1}^{N}\int_0^\infty d^2\underline{k}\left[u(\underline{k})e^{i\underline{k}\cdot\underline{R}_n}cos(\theta_n) + v(\underline{k})e^{i\underline{k}\cdot\underline{R}_n}sin(\theta_n)\right]. \tag{9}$$

Assuming statistical homogeneity and stationarity conditions, frequency spectral estimates $S_{\overline{HD}}(\omega; R, N)$ can be written as

$$\begin{aligned} S_{\overline{HD}}(\omega; R, N) = \; & \frac{4}{N^2R^2}\sum_{n=1}^{N}\sum_{n'=1}^{N}\int_0^\infty d\underline{k}^2 e^{i\underline{k}\cdot(\underline{R}_n-\underline{R}_{n'})} \\ & \{P_{uu}(\underline{k},\omega)cos(\theta_n)cos(\theta_{n'}) + P_{vv}(\underline{k},\omega)sin(\theta_n)sin(\theta_{n'}) \\ & + P_{uv}(\underline{k},\omega)cos(\theta_n)sin(\theta_{n'}) + P_{vu}(\underline{k},\omega)sin(\theta_n)cos(\theta_{n'})\}. \end{aligned} \tag{10}$$

Here, $P_{uu}(\underline{k},\omega)$, $P_{vv}(\underline{k},\omega)$, $P_{vu}(\underline{k},\omega)$, and $P_{uv}(\underline{k},\omega)$ are wavenumber–frequency autospectra of u and v, and wavenumber–frequency co–spectra between u and v. Assuming a horizontally isotropic flow field, velocity frequency spectra at a given space lag $(\underline{R}_n - \underline{R}_{n'})$ can be expressed as

$$\begin{aligned} P_{uu}(\omega; \underline{R}_n - \underline{R}_{n'}) = \; & \int_0^\infty d\alpha \left\{[J_0(\alpha r) + cos(\theta_n + \theta_{n'})J_2(\alpha r)]\frac{S_{HD}(\alpha,\omega)}{2\alpha^2}\right. \\ & \left. + [J_0(\alpha r) - cos(\theta_n + \theta_{n'})J_2(\alpha r)]\frac{S_{RV}(\alpha,\omega)}{2\alpha^2}\right\}, \end{aligned} \tag{11}$$

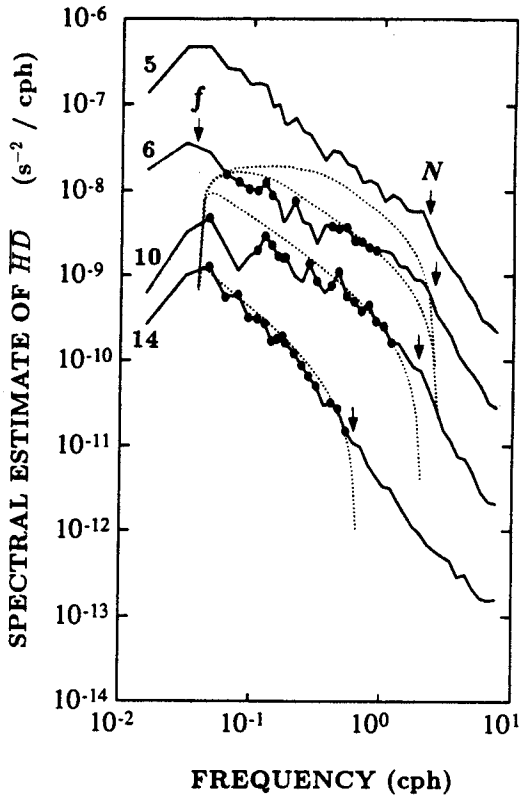

Figure 3. Observed frequency spectra of horizontal divergence at four IWEX levels (solid lines) and comparison with the GM-76 spectrum model (dotted lines). The attenuation and contamination array response functions have been applied to the GM model. Solid circles show agreement between observed spectral estimates and the GM model within 95% confidence interval.

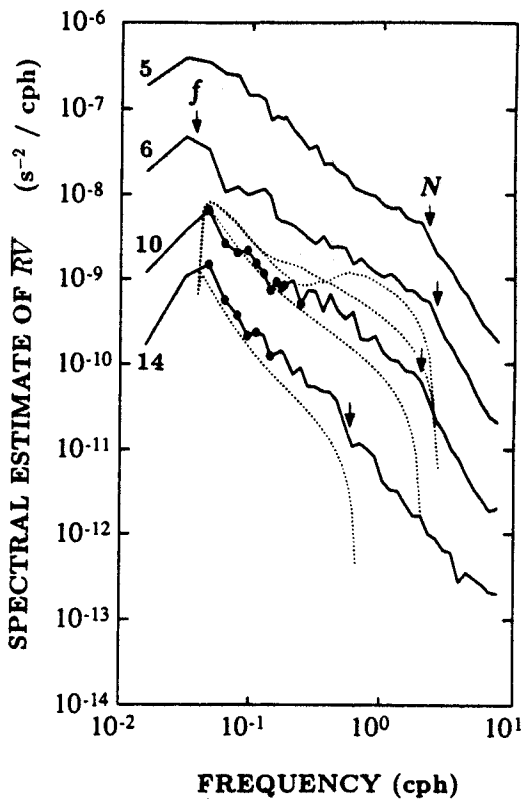

Figure 4. Observed frequency spectra of relative vorticity at four IWEX levels (solid lines) and comparison with the GM-76 spectrum model (dotted lines). The attenuation and contamination array response functions have been applied to the GM model. Solid circles show agreement between observed spectral estimates and the GM model within 95% confidence interval.

$$P_{vv}(\omega;\underline{R}_n-\underline{R}_{n'}) = \int_0^\infty d\alpha \left\{ [J_0(\alpha r) - cos(\theta_n+\theta_{n'})J_2(\alpha r)] \frac{S_{HD}(\alpha,\omega)}{2\alpha^2} + [J_0(\alpha r) + cos(\theta_n+\theta_{n'})J_2(\alpha r)] \frac{S_{RV}(\alpha,\omega)}{2\alpha^2} \right\}, \tag{12}$$

$$P_{uv}(\omega;\underline{R}_n-\underline{R}_{n'}) = P_{vu}(\omega;\underline{R}_n-\underline{R}_{n'}) = \int_0^\infty d\alpha J_2(\alpha r) sin(\theta_n+\theta_{n'}) \frac{S_{HD}(\alpha,\omega)-S_{RV}(\alpha,\omega)}{2\alpha^2}, \tag{13}$$

where $r = 2\alpha R sin(\frac{\theta_n - \theta_{n'}}{2})$, and α is the magnitude of horizontal wavenumber (after Batchelor, 1953). J_0 and J_2 are Bessel functions of zeroth and second orders.

Therefore, the frequency spectral estimate $S_{\overline{HD}}(\omega; R, N)$ can be expressed in terms of real wavenumber–frequency spectra $S_{HD}(\alpha,\omega)$ and $S_{RV}(\alpha,\omega)$ as

$$S_{\overline{HD}}(\omega; R, N) = \int_0^\infty d\alpha \left\{ S_{HD}(\alpha,\omega) F(\alpha R, N) + S_{RV}(\alpha,\omega) G(\alpha R, N) \right\}. \tag{14}$$

Similarly, the frequency spectral estimate of area–averaged relative vorticity can be expressed as

$$S_{\overline{RV}}(\omega; R, N) = \int_0^\infty d\alpha \left\{ S_{RV}(\alpha,\omega) F(\alpha R, N) + S_{HD}(\alpha,\omega) G(\alpha R, N) \right\}, \tag{15}$$

where

$$\begin{aligned} F(\alpha R, N) = \; & \frac{2}{N^2 \alpha^2 R^2} \sum_{n=1}^{N} \sum_{n'=1}^{N} \\ & \left[cos(\theta_n - \theta_{n'}) J_0 \left(2\alpha R sin(\frac{\theta_n - \theta_{n'}}{2}) \right) + J_2 \left(2\alpha R sin(\frac{\theta_n - \theta_{n'}}{2}) \right) \right], \end{aligned} \tag{16}$$

and

$$\begin{aligned} G(\alpha R, N) = \; & \frac{2}{N^2 \alpha^2 R^2} \sum_{n=1}^{N} \sum_{n'=1}^{N} \\ & \left[cos(\theta_n - \theta_{n'}) J_0 \left(2\alpha R sin(\frac{\theta_n - \theta_{n'}}{2}) \right) - J_2 \left(2\alpha R sin(\frac{\theta_n - \theta_{n'}}{2}) \right) \right]. \end{aligned} \tag{17}$$

For the IWEX configuration ($N = 3$), two array response functions have the form of

$$F(\alpha R) = \frac{2}{3\alpha^2 R^2} \left[1 - J_0(\sqrt{3}\alpha R) + 2J_2(\sqrt{3}\alpha R) \right], \tag{18}$$

$$G(\alpha R) = \frac{2}{3\alpha^2 R^2} \left[1 - J_0(\sqrt{3}\alpha R) - 2J_2(\sqrt{3}\alpha R) \right]. \tag{19}$$

Array response functions $F(\alpha R, N)$ and $G(\alpha R, N)$ are displayed in Figures 5 and 6 for cases of three, nine, and an infinite number of current sensors ($N = 3, 9$, and ∞) along a circle on a horizontal plane. The array response function F behaves as a lowpass wavenumber filter representing the effect of the finite size of the circle. Fluctuations of horizontal divergence and relative vorticity at scales smaller than the size of the circle are attenuated in our estimates. Therefore, F is termed the attenuation array response function. Note that increasing the number of current sensors on the circle cannot eliminate the attenuation problem. The array response function G behaves as a bandpass wavenumber filter. Fluctuations of horizontal divergence and relative vorticity are mutually contaminated in our estimates at horizontal scale comparable to the sensor separation since the tangential and normal components of horizontal velocity at scale smaller than the sensor separation is not detectable. The peak of the contamination array response function moves to higher wavenumber (smaller horizontal scale) and its magnitude is reduced with the increasing number of current sensors on the circle. In the ideal case of an infinite number of current sensors on the circle, the contamination array response function vanishes.

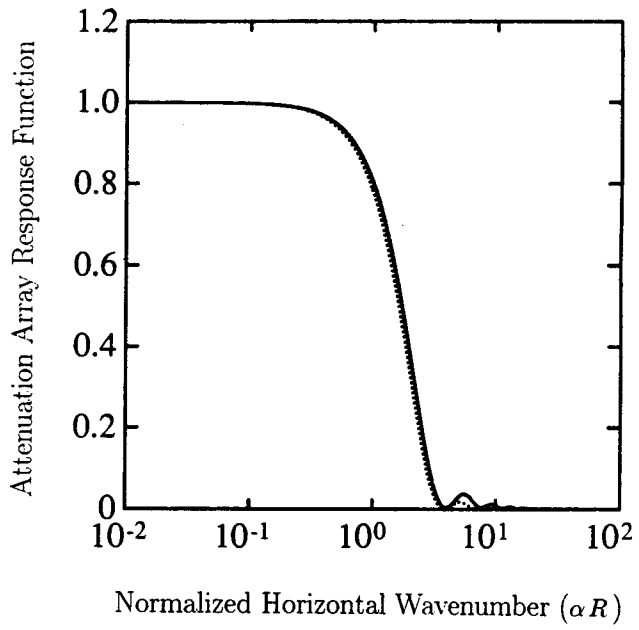

Figure 5. Attenuation array response function for cases of 3 (solid line), 9 (dotted line), and an infinite number of current sensors on a horizontal plane. For the case of an infinite number of current sensors, $F(\alpha R) = 4J_1^2(\alpha R)/(\alpha R)^2$, and it is not distinguishable from the case of 9 current sensors.

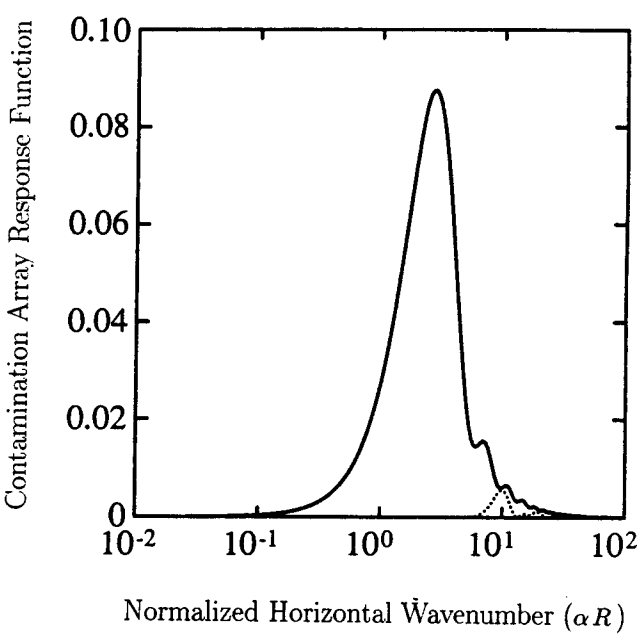

Figure 6. Contamination array response function for cases of 3 (solid line), 9 (dotted line), and an infinite number of current sensors on a horizontal plane. For the case of an infinite numbter of current sensors, the contamination array response function vanishes.

Effects of Array Response Functions for GM–76 Spectrum

Using the polarization relation of internal waves, frequency spectra $S_{\overline{HD}}(\omega; R, N = 3)$ and $S_{\overline{RV}}(\omega; R, N = 3)$ of the GM–76 spectrum model (Cairns and Williams, 1976) are obtained. Effects of array response functions (see equations 18 and 19) are evaluated employing the wavenumber structure of the GM model in which a vertical cutoff wavenumber of 0.1 cpm is assigned.

Characteristic wavenumbers of the attenuation and contamination array response functions are estimated (Table 2) which vary for different array sizes and sensor separations at four IWEX levels. Note that the characteristic wavenumbers are the property of array response functions, and do not depend on the GM model. Applying the vertical cutoff wavenumber prescribed in the GM model and the dispersion relation of linear internal waves, frequency regimes (Table 2) are identified in which the GM spectrum is affected by array response functions.

The effects of array response functions for the GM model are illustrated in Figures 7 and 8 in which horizontal divergence and relative vorticity frequency spectra of the GM model at IWEX level 10 are estimated. In the absence of array response functions, the horizontal divergence and relative vorticity frequency spectra of the GM model have zero and –2 spectral slopes, respectively. By incorporating the attenuation array response functions, equivalent to area–averaging horizontal divergence and relative vorticity on a circle, frequency spectral slopes of horizontal divergence and relative vorticity become steeper. Since high frequency waves are associated with high wavenumbers whose fluctuations are attenuated, the attenuation is more apparent in the high frequency regime. Including the contamination from relative vorticity, the GM frequency spectrum of horizontal divergence is not significantly modified since the spectral ratio of relative vorticity to horizontal divergence is f^2/ω^2 for linear internal waves. On the contrary, the GM frequency spectrum of relative vorticity is markedly modified because of the contamination from horizontal divergence (Figure 8). Agreements between observed frequency spectra of horizontal divergence and relative vorticity with the corresponding GM spectra are greatly improved by including attenuation and contamination array response functions in the model. Both array response functions must be considered in the calculation of relative vorticity frequency spectrum of the GM model, whereas only the attenuation array response function is important to estimate the horizontal divergence spectrum of the GM model. The comparison of observed frequency spectra of horizontal divergence and relative vorticity with the corresponding GM model including both array response functions at all four levels is presented in Figures 3 and 4. Note that the GM model predicts $\overline{HD}$ much better than $\overline{RV}$. This discrepancy might be due to the existence of vortical motion, which has RV but no HD, or due to the inadequacy of the GM model. This issue is more fully discussed by Lien and Müller (1991).

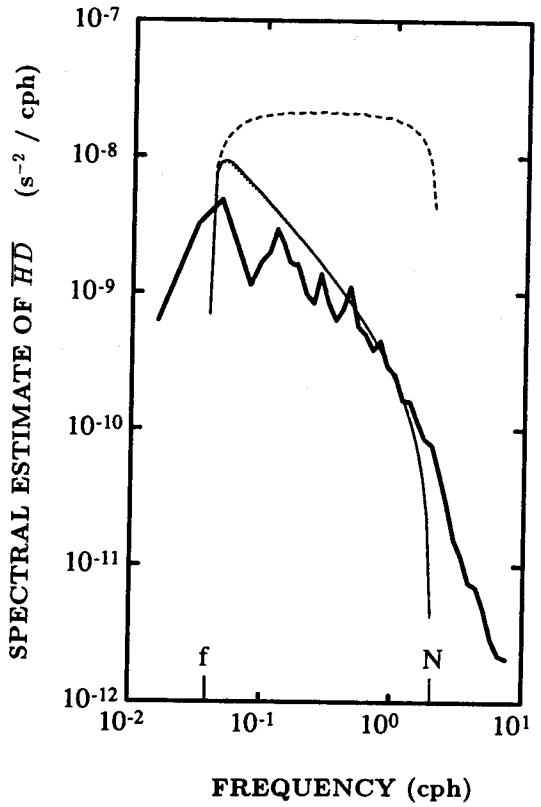

Figure 7. Effects of array response functions on the GM-76 spectrum. The thick solid line denotes the frequency spectral estimate $S_{\overline{HD}}(\omega)$ at IWEX level 10. The GM horizontal divergence spectrum in the absence of attenuation and contamination effects is shown by the dashed line. The dotted line is the horizontal divergence spectrum of the GM model including the attenuation effect, and the thin solid line includes both the attenuation and contamination effects. The dotted and the thin solid lines are not distinguishable.

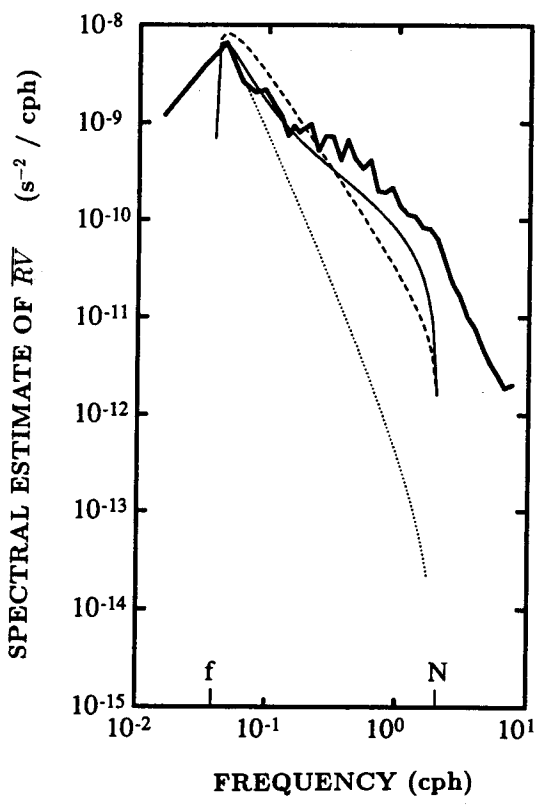

Figure 8. Effects of array response functions on the GM-76 spectrum. The thick solid line denotes the frequency spectral estimate $S_{\overline{RV}}(\omega)$ at IWEX level 10. The GM relative vorticity spectrum in the absence of attenuation and contamination effects is shown by the dashed line. The dotted line is the relative vorticity spectrum of the GM model including the attenuation effect, and the thin solid line includes both the attenuation and contamination effects.

SUMMARY AND DISCUSSION

The estimation of horizontal divergence and relative vorticity is motivated by the need to conveniently project small–scale motion into the gravity and vortical modes using the normal mode decomposition. This paper addresses the practical problems of estimating horizontal divergence and relative vorticity using discrete sampling in space of horizontal velocity measurements.

Table 2. Characteristic horizontal wavenumbers of array response functions and the corresponding frequencies obtained by assuming the dispersion relation of linear internal waves and the vertical cutoff wavenumber β_c of 0.1 cpm. The attenuation array response function drops to 0.90 at α_t, and decreases with increasing horizontal wavenumber by a -2 power law. Frequency spectra of $\overline{HD}$ and $\overline{RV}$ are affected by the attenuation array response function at frequencies greater than $\omega_t(=\sqrt{[N^2\alpha_t^2+f^2\beta_c^2]/[\alpha_t^2+\beta_c^2]})$. At lower frequencies, there is no attenuation effect. The contamination array response function behaves as a bandpass filter with its peak at α_c with an amplitude about 0.1, and decreases at a -2 power law away from α_c. Frequency spectra of $\overline{HD}$ and $\overline{RV}$ do not have significant effects of contamination array response function at frequencies smaller than $\omega_c,(=\sqrt{[N^2\alpha_c^2+f^2\beta_c^2]/[\alpha_c^2+\beta_c^2]})$.

Level	α_t (cpm)	ω_t (cph)	α_c (cpm)	ω_c (cph)
5	6.3×10^{-3}	0.12	1.7×10^{-2}	0.44
6	2.0×10^{-3}	0.05	5.4×10^{-3}	0.15
10	6.0×10^{-4}	0.04	1.7×10^{-3}	0.05
14	2.0×10^{-4}	0.04	5.0×10^{-4}	0.04

There are two types of sampling errors in the estimation of horizontal divergence and relative vorticity. Fluctuations of horizontal divergence and relative vorticity are attenuated and mutually contaminated at smaller horizontal scales corresponding to the array size and the sensor separation. Decontamination requires horizontal wavenumber structures of horizontal divergence and relative vorticity, which are not yet available. Moreover, the contamination problem causes the normal mode decomposition to be infeasible using IWEX measurements (Lien, 1990).

Effects of array response functions were examined using the GM–76 spectrum model. It was found that both the attenuation and contamination error should be considered in the calculation of the relative vorticity spectrum. Since the variance of relative vorticity is much smaller than that of horizontal divergence for linear internal waves (except on the inertial frequency), only the attenuation effect needs to be considered in obtaining the horizontal divergence spectrum, and the contamination from the relative vorticity is negligible.

ACKNOWLEDGMENTS:

We would like to thank Dr. Eric Kunze, Mark Prater and Niklas Schneider for stimulating discussions and constructive ideas. We are also grateful to Diane Henderson and Twyla Thomas for their editorial assistance. This research is supported by the Office of Naval Research.

REFERENCES:

Batchelor, G. K., 1953: The theory of homogeneous turbulence, Cambridge University Press, 197 pp.

Briscoe, M. G., 1975: Preliminary results from the trimoored internal wave experiment (IWEX), J. Geophys. Res., 80, 27, 3872–3884.

Cairns, J. L., and G. D. Williams, 1976: Internal wave observations from a midwater float, Part II, J. Geophys. Res., 81, 1943–1950.

Kunze, E., A. J. Williams, III and M. G. Briscoe, 1990: Interpreting shear and strain finestructure from a neutrally–buoyant float, J. Geophys. Res., 95, 18111–18125.

Lien, R.–C., 1990: Normal mode decomposition of small–scale oceanic motions, Ph.D. Dissertation, University of Hawaii at Manoa. 128 pp.

Lien, R.–C. and P. Müller, 1991: Normal mode decomposition of small–scale oceanic motions, submitted to J. Phys. Oceanogr.

Müller, P., 1984: Small scale vortical motions. Internal Gravity Waves and Small-Scale Turbulence, Proc., 'Aha Huliko'a Hawaiian Winter Workshop, Hawaii Institute of Geophys., Spec. Pub., P. Müller and R. Pujalet, Eds.

Müller, P., R. C. Lien, and R. Williams, 1988: Estimates of potential vorticity at small scales in the ocean, J. Phys. Oceanogr., 18, 401–416.

Prater, M. D., 1989: Simulations of flow past a triad of current meters, Unpublished manuscript.

Tarbell, S. M., M. G. Briscoe, and D. Chausse, 1976: A compilation of moored current data and associated oceanographic observations, 1973 Internal Wave Experiment (IWEX), Tech. Rep., 75–68, Vol. IX, Woods Hole Oceanogr. Inst., Woods Hole, MA.